INTERNATIONAL JOURNAL FOR NUMERICAL METHODS IN FLUIDS
Int. J. Numer. Meth. Fluids 2003; **41**:419–445 (DOI: 10.1002/fld.448)

A domain decomposition approach to compute wave breaking (wave-breaking flows)

A. Iafrati*,† and E. F. Campana

INSEAN - Istituto Nazionale per Studi ed Esperienze di Architettura Navale - Via di Vallerano, 139-00128-Roma, Italy

SUMMARY

A heterogeneous domain decomposition approach is followed to simulate the unsteady wavy flow generated by a body moving beneath a free surface. Attention being focused on complex free surface configurations, including wave-breaking phenomena, a two-fluid viscous flow model is used in the free surface region to capture the air–water interface (via a level-set technique), while a potential flow approximation is adopted to describe the flow far from the interface. Two coupling strategies are investigated, differing in the transmission conditions. Both the adopted approaches make use of the inviscid velocity field as boundary condition in the Navier–Stokes solution.
For validation purposes, two different two-dimensional non-breaking flows are simulated. Domain decomposition results are compared with both fully viscous and fully inviscid results, obtained by solving the corresponding equations in the whole fluid domain, and with available experimental data. Finally, the unsteady evolution of a steep breaking wave is followed and some of the physical phenomena, experimentally observed, are reproduced. Copyright © 2003 John Wiley & Sons, Ltd.

KEY WORDS: domain decomposition; level set; free surface flow; wave breaking

1. INTRODUCTION

In this paper, a heterogeneous domain decomposition approach to compute unsteady water waves is developed. Since attention is mainly oriented to the analysis of the most relevant phenomena produced by a breaking wave, including the entrainment of air in water, a two-fluid Navier–Stokes solver [1] is used to describe the fluid dynamics in the interface vicinities. Far from this region the flow is assumed irrotational, thus allowing the use of potential flow models.

* Correspondence to: A. Iafrati, Istituto Nazionale per Studi ed Esperienze di Architettura Navale, Via di Vallerano, 139-00128 Roma, Italy.
† E-mail: a.iafrati@insean.it

Contract/grant sponsor: Office of Naval Research; contract/grant number: N000140010344
Contract/grant sponsor: Ministero delle Infrastrutture e dei Transporti; contract/grant number: INSEAN Research Plan 2000-02

Received February 2002
Revised 26 August 2002

The motivation for this work stems from the difficulty in modelling the complex flow generated by an advancing surface ship. The motion of a marine vehicle travelling on the sea surface, beside producing a system of transversal water waves, usually leads to the formation of spray from the bow and the generation of steep diverging bow and stern waves, possibly breaking. As a consequence of the overturning, a sequel of interesting phenomena follow: the generation of vorticity in the breaking region, the downstream propagation of a shear layer close to the free surface, the entrainment of air in water, and the intense bubbly flow propagating along the side of the hull toward the stern region, eventually being convected into the wake.

Much of the literature dedicated to the subject is of theoretical [2] or experimental nature [3], the numerical investigation requiring too expensive techniques and highly refined grids to manage the complicated interface topologies. Due to this problem, numerical works have been confined for some time to the use of irrotational flow models, used to analyse the early stages of the breaking [4, 5]. In recent years, the discrete treatment of interfacial flows displayed a considerable progress, and several numerical schemes, that can be efficiently coupled with Navier–Stokes solvers, have been developed, as discussed in Reference [6]. However, a complete solution of the unsteady Navier–Stokes equations past a full-scale ship, with the grid refinement required for capturing these phenomena, is actually beyond the available computational resources. On the other hand, a careful description of the flow is only needed in a small neighbourhood of the interface while the underwater flow is rather smooth and can be described by much simpler techniques, hence pushing toward the design of domain decomposition methods.

In the naval context, the use of these approaches has been mostly confined in the framework of the free surface steady flow, e.g. References [7, 8]. In these works, attention was mainly focused in the evaluation of viscous effects on the ship resistance completely disregarding wave breaking phenomena.

The present study is dedicated to the development of an unsteady, heterogeneous, domain decomposition method, which couples viscous and inviscid flow models, aimed at the simulation of breaking water waves. The whole fluid domain is subdivided in two regions, one encompassing the interface location and the other one beneath. In the free surface region the unsteady two-fluid Navier–Stokes equations are solved and a level-set technique [9] is adopted to capture the interface motion. The velocity field is assumed to be assigned all along the boundary. In the bottom domain, a boundary integral representation of the velocity potential is used with Neumann boundary conditions on the body contour and at the inflow and outflow sections.

Attention is devoted to the correct coupling of the two subdomains and two different strategies are developed by changing the boundary condition applied at the matching surface from the upper domain. The first approach, Neumann type (NT), is based on a Schwarz alternating method [10, 11] and uses the normal velocity obtained from the Navier–Stokes solver to assign the normal derivative of the velocity potential at the matching surface. The second one, Dirichlet type (DT), uses the normal stress of the Navier–Stokes solver as a pressure field acting on the bottom part of the domain. This pressure field is used within the unsteady Bernoulli's equation to recover the distribution of the velocity potential on the matching surface. Regardless the way used to couple the two domains, the solution of the boundary value problem in the bottom domain provides the velocity field on the matching surface to be used as boundary condition for the Navier–Stokes solver. Subiterations are included to achieve the

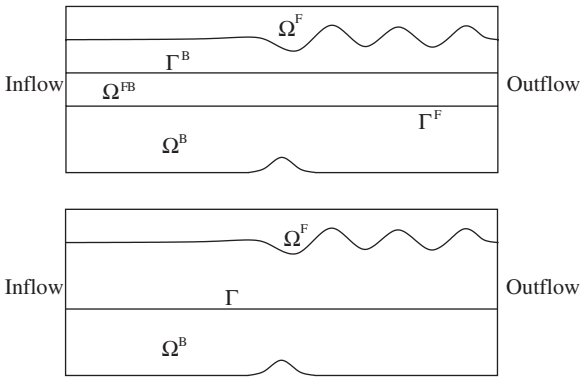

Figure 1. Sketch of the subdivision of the fluid domain used for the two different domain decomposition approaches: NT (*top*) and DT (*bottom*).

solutions in the two domains at the same time. It is worth to remark that, although the methods are here applied only to two-dimensional (2D) problems, they can be directly extended to three-dimensional (3D) flows.

For validation purposes, the developed approaches are initially applied to the non-breaking wavy flow generated by a bump moving on the bottom of a channel. Comparisons with solutions obtained using the Navier–Stokes solver in the whole fluid domain are established, and a careful verification of the results is also presented. The time evolution of a steep water wave, produced by a submerged hydrofoil, eventually breaking, is finally investigated and some of the relevant phenomena experimentally observed are recovered by the numerical solution.

2. DOMAIN DECOMPOSITION APPROACH

When dealing with complex free surface flows, such as wave breaking, significant viscous effects and vorticity production are induced near entrained air bubbles, in region with highly curved interface or in region where high velocity gradient are originated as a consequence of the impacting process. Far deeper, stronger approximation can be made about the flow properties and then simpler models can be employed. Hence, the interest behind the use of a heterogeneous domain decomposition approach lies in the expectation of a better use of the computational resources when employing the most suitable numerical technique in different subregions of the whole fluid domain. A rigorous mathematical discussion of heterogeneous models, along with some examples, is reported in Reference [11, Chapter 8] and references therein.

In the case of regular waves, the wavy flow induced by bodies moving beneath the interface, can be described, rather accurately, by potential flow models, in spite of the strong approximations made about the flow field in the body vicinities. This suggested the idea to couple the Navier–Stokes solver, developed to face complex free surface flows [1], with a boundary element solver [12]. Consequently, the whole fluid domain is split into an upper (free surface region) and a deeper (bottom region) subdomain, as shown in Figure 1. Depending on the coupling procedure adopted, an overlapping between the two subdomains, leading to a finite thickness of the matching region, may be required to allow the advancement in time.

Two different strategies are used to couple the two models. In the first one, the two subdomains are partially overlapped and the normal velocity component at the upper matching surface is used as Neumann boundary condition for the potential solver. The second way of coupling uses the pressure at the matching surface to get the source term for the unsteady Bernoulli's equation. Time integration of the Bernoulli's equation provides the velocity potential to be used as Dirichlet boundary condition for the potential solver. For the latter approach there is no need of overlapping. Regardless the boundary condition used for the potential flow model in the bottom subdomain, both velocity components are assigned to the Navier–Stokes solver all along the boundary of the free surface subdomain. In order to clarify the coupling procedures of the domain decomposition, a detailed description of the governing equations, together with the appropriate boundary conditions, is given in the following.

2.1. The governing equations

The unsteady Navier–Stokes solver, coupled with a level-set method [9], is used to describe the complex interface topologies that may take place in the free surface region Ω^{F}. In the bottom region Ω^{B} the flow is assumed to be inviscid and irrotational and a potential model is therefore adopted. In both cases an incompressible fluid is assumed. The flow is observed in a frame of reference (x_1, x_2) attached to the body, which is moving with a steady speed $\mathbf{V}$ from the right to the left.

Concerning with the governing equations, in the free surface region Ω^{F}, the flow is described by the Navier–Stokes equations written for an incompressible fluid having variable density and viscosity:

$$\nabla \cdot \mathbf{u} = 0 \tag{1}$$

$$\frac{D\mathbf{u}}{Dt} = -\frac{1}{\rho}\nabla p_{\mathrm{F}} + \mathbf{f} + \frac{1}{\rho}\nabla \cdot [\mu(\nabla \mathbf{u} + \nabla \mathbf{u}^{\mathrm{T}})] + \sigma\kappa\boldsymbol{\nu}\delta(\mathbf{x} - \mathbf{x}_s) \tag{2}$$

Here $\mathbf{u}$ is the fluid velocity, ρ and μ are the local values of density and dynamic viscosity, p_{F} is the pressure, $\mathbf{f}$ denotes the mass forces, σ is the surface tension coefficient, κ is the local curvature of the interface and $\boldsymbol{\nu}$ is the unit normal vector at the interface oriented toward the air. In (2) the term $\delta(\mathbf{x} - \mathbf{x}_s)$ represents the Dirac function which is zero out of the interface location $\mathbf{x}_s$.

All along the boundary of the upper subdomain, the two velocity components are assigned. In particular it is assumed

$$(u_1, u_2) = (1, 0) \quad \text{on } \partial\Omega_{\mathrm{I}}^{\mathrm{F}} \cup \partial\Omega_{\mathrm{O}}^{\mathrm{F}} \cup \partial\Omega_{\mathrm{T}}^{\mathrm{F}} \tag{3}$$

where $\partial\Omega_{\mathrm{I}}^{\mathrm{F}}, \partial\Omega_{\mathrm{O}}^{\mathrm{F}}$ denote the inflow and outflow sections and $\partial\Omega_{\mathrm{T}}^{\mathrm{F}}$ is the upper boundary of the free surface subdomain, located in the air. The boundary condition along the matching surface is discussed later on.

In the bottom region, Ω^{B}, the flow field is recovered in terms of a velocity potential φ which satisfies the Laplace equation

$$\Delta\varphi = 0 \tag{4}$$

Neumann boundary conditions are applied on the inflow and outflow sections and on the bottom contour of the channel ($\partial\Omega_B^B$):

$$\frac{\partial\varphi}{\partial n} = 1 \quad \text{on } \partial\Omega_I^B \tag{5}$$

$$\frac{\partial\varphi}{\partial n} = -1 \quad \text{on } \partial\Omega_O^B \tag{6}$$

$$\frac{\partial\varphi}{\partial n} = 0 \quad \text{on } \partial\Omega_B^B \tag{7}$$

Different boundary conditions are applied at the matching surface depending on the strategy adopted for the coupling.

2.2. *The Neumann type coupling* (*NT*)

This kind of approach is substantially based on a Schwarz alternating method [10, 11]. The two subdomains are overlapped (Figure 1(a)) and the normal velocity component, obtained from the Navier–Stokes solver on $\Gamma^B := \partial\Omega^B \cap \Omega^F$, is used as Neumann boundary condition in the potential solver. The solution of the boundary value problem in the bottom subdomain gives back the velocity field along $\Gamma^F := \partial\Omega^F \cap \Omega^B$ which is used as boundary condition for the Navier–Stokes solver. Formally,

$$(u_1, u_2) = (u_1^B, u_2^B) \quad \text{on } \Gamma^F \tag{8}$$

$$\frac{\partial\varphi}{\partial n} = \mathbf{u}^F \cdot \mathbf{n} \quad \text{on } \Gamma^B \tag{9}$$

Subiterations are performed to obtain convergence in terms of the velocity component on Γ^F. The coupling procedure at the time step $t \to t + \Delta t$ is the following:

- the Navier–Stokes equations are advanced in time from t to $t + \Delta t$ by using $\mathbf{u}^B(t)$ as boundary condition on the matching surface Γ^F;
- the tentative velocity field at the new time step is used to get the normal velocity component at Γ^B;
- the Laplace equation is solved in Ω^B;
- the two velocity components (u_1^B, u_2^B) are evaluated on Γ^F and used as boundary conditions for the Navier–Stokes solver at the next iteration;
- iterations are repeated till a convergence criteria is satisfied.

2.3. *The Dirichlet type coupling* (*DT*)

In the above described approach, the solution in the bottom subdomain simply enforces a kinematic constraint. A different way of coupling can be developed by solving the corresponding dynamic problem also in the bottom region. Unlikely from the previous one, the overlapping between the subdomains is not needed in this case, thus $\Gamma^F \equiv \Gamma^B = \Gamma$ (Figure 1(b)).

Within the potential flow approximation, the unsteady Bernoulli's equation governs the dynamics in Ω^{B}. So, this coupling procedure uses the normal stresses at the matching surface as a forcing pressure field. This is a source term for the unsteady Bernoulli's equation which is integrated in time to get the distribution of the velocity potential along the matching surface to be used as a Dirichlet boundary condition for the Laplace problem. The latter provides the distribution of the velocity component normal on Γ, while the distribution of the tangential component can be directly computed by the tangential derivative of the velocity potential along the matching surface.

The boundary conditions on the matching surface Γ reads then

$$(u_1, u_2) = (u_1^{\mathrm{B}}, u_2^{\mathrm{B}}) \tag{10}$$

$$\varphi = \int_0^t \left(\frac{\partial \varphi}{\partial t}\right) \mathrm{d}t = \int_0^t \left(-\frac{p_{\mathrm{B}}}{\rho} - g x_2 - \frac{|\mathbf{u}^{\mathrm{F}}|^2}{2}\right) \mathrm{d}t \tag{11}$$

for the upper and lower subdomains, respectively, g being the gravity acceleration. To enforce the continuity of the normal stresses at the matching surface, the pressure used in the bottom subdomain, p_B, is related to that in the free surface region, p_{F}, by the relation

$$p_{\mathrm{B}} = p_{\mathrm{F}} - 2\mu \frac{\partial u_n}{\partial n}$$

In the numerical procedure the Bernoulli equation is integrated in time within the Runge–Kutta scheme adopted for the integration in time of the Navier–Stokes equations. In this case, the advancement in time between t and $t + \Delta t$ is carried out in three substeps. Let $2\alpha(i)\Delta t$ denote the time advance of the ith Runge–Kutta substep, the integration in time of the velocity potential is written as

$$\varphi(t_i + 2\alpha(i)\Delta t) = \varphi(t_i) + \alpha(i) \left(\frac{\partial \varphi}{\partial t}(t_i) + \frac{\partial \varphi}{\partial t}(t_i + 2\alpha(i)\Delta t)\right) \Delta t \tag{12}$$

where t_i is the initial time of the ith Runge–Kutta substep, with $t_1 = t$. Since the value of $\partial\varphi/\partial t$ at the end of the substep is unknown, an iterative procedure is used as described below:

- from the solution at t_i, the pressure and the velocity field at the matching line can be used to get $\partial\varphi/\partial t(t_i)$;
- the Navier–Stokes equation is advanced in time from t_i to $t_i + 2\alpha(i)\Delta t$ by using $\mathbf{u}^{\mathrm{B}}(t_i)$ as boundary condition at the matching surface;
- from the solution of the Navier–Stokes equation, an estimate of the normal stress along the matching surface at $t_i + 2\alpha(i)\Delta t$ is recovered and used to get an approximate value for $\partial\varphi/\partial t$ at $t_i + 2\alpha(i)\Delta t$;
- the latter provides $\varphi(t_i + 2\alpha(i)\Delta t)$ via (12) and then, by solving the Laplace problem, the new estimate of the velocity at the matching surface can be obtained to be used as boundary conditions for the Navier–Stokes solver at the next iteration;
- iterations are repeated till a convergence criteria is not satisfied.

3. MATHEMATICAL MODEL AND NUMERICAL ALGORITHM

3.1. Navier–Stokes solver in generalized co-ordinates

The flow of air and water is approximated as that of a single incompressible fluid whose density and viscosity smoothly change across the interface. With this assumption, in an Eulerian frame of reference, local fluid properties vary with time only due to the interface motion, and the continuity equation in generalized co-ordinates simply reads

$$\frac{\partial U_m}{\partial \xi_m} = 0 \tag{13}$$

where

$$U_m = J^{-1} \frac{\partial \xi_m}{\partial x_j} u_j \tag{14}$$

is the volume flux normal to the ξ_m iso-surface and J^{-1} is the inverse of the Jacobian.

In order to include surface tension effects in the momentum equation, the continuum modeling, suggested by Brackbill *et al.* [13] and recently employed also by Sussman and Puckett [14], is used. Since a level-set technique is used to capture the interface location, the signed normal distance from the interface d is assumed to be the 'colour function' [13]. Hence, the momentum equation, in non-dimensional form, is

$$\begin{aligned} \frac{\partial}{\partial t}(J^{-1}u_i) + \frac{\partial}{\partial \xi_m}(U_m u_i) = & -\frac{1}{\varrho}\frac{\partial}{\partial \xi_m}\left(J^{-1}\frac{\partial \xi_m}{\partial x_i}\, p_{\mathrm{F}}\right) - J^{-1}\frac{\delta_{i2}}{Fr^2} \\ & - \frac{\kappa}{\varrho\, We^2}\frac{\partial}{\partial \xi_m}\left(J^{-1}\frac{\partial \xi_m}{\partial x_i} H(d)\right) \\ & + \frac{1}{\varrho\, Re}\frac{\partial}{\partial \xi_m}\left(\mu G^{ml}\frac{\partial u_i}{\partial \xi_l} + \mu B^{mlji}\frac{\partial u_j}{\partial \xi_l}\right) \end{aligned} \tag{15}$$

where u_i is the ith Cartesian velocity component, δ_{ij} is the Kronecker delta and

$$Fr = \frac{U_{\mathrm{r}}}{\sqrt{gL_{\mathrm{r}}}}, \quad Re = \frac{U_{\mathrm{r}} L_{\mathrm{r}} \varrho_w}{\mu_w}, \quad We = U_{\mathrm{r}}\sqrt{\frac{\varrho_w L_{\mathrm{r}}}{\sigma}} \tag{16}$$

are the Froude, Reynolds and Weber numbers, respectively. Here, U_{r}, L_{r} are reference values for velocity and length, σ is the surface tension coefficient while ϱ_w, μ_w are the values of density and dynamic viscosity in water and are used as reference values. In (15)

$$G^{ml} = J^{-1}\frac{\partial \xi_m}{\partial x_j}\frac{\partial \xi_l}{\partial x_j}, \qquad B^{mlji} = J^{-1}\frac{\partial \xi_m}{\partial x_j}\frac{\partial \xi_l}{\partial x_i} \tag{17}$$

are metric quantities, κ is the local curvature and $H(d)$ is the Heaviside function. According to the definitions reported in the next section, the distance function d is positive in water and negative in air, so that $H(d)=1$ in water and $H(d)=0$ in air.

The numerical solution of the Navier–Stokes equations is achieved through a finite volume solver on a non-staggered grid. The grid layout and the numerical approach are similar to those suggested by Zang *et al.* [15]: cartesian velocities and pressure are defined at the cell centres whereas volume fluxes are defined at the mid point of the cell faces. A fractional step approach is employed: the momentum equation is advanced in time by neglecting pressure terms (*Predictor step*) whose effects are successively reintroduced by enforcing the continuity of the velocity field (*Corrector step*). The diagonal part of the dominating diffusive terms, i.e. that originated from $\nabla\mathbf{u}$, are accounted implicitly with a Crank–Nicolson scheme, whereas all the other terms are computed explicitly. With respect to Reference [15], a three-steps Runge–Kutta scheme [16] is adopted here. The grid being fixed in time, the discretized form of the momentum equation at the step n is

Step 1:

$$(J^{-1}-\alpha_1\Delta t D_{\mathrm{I}})\frac{(\hat{u}_i^1-u_i^n)}{\Delta t}=\gamma_1[C(u_i^n)+D_{\mathrm{E}}(u_i^n)+T_i(d^n)]+2\alpha_1\left[-J^{-1}\frac{\delta_{i2}}{Fr^2}+D_{\mathrm{I}}(u_i^n)\right]$$

$$\tilde{u}_i^1-\hat{u}_i^1=\gamma_1\frac{R_i(\tilde{\phi}^1)}{\tilde{\varrho}^1J^{-1}}$$

Step 2:

$$(J^{-1}-\alpha_2\Delta t D_{\mathrm{I}})\frac{(\hat{u}_i^2-\tilde{u}_i^1)}{\Delta t}=\gamma_2[C(\tilde{u}_i^1)+D_{\mathrm{E}}(\tilde{u}_i^1)+T_i(\tilde{d}^1)]+\zeta_1[C(u_i^n)+D_{\mathrm{E}}(u_i^n)+T_i(d^n)]+2\alpha_2\left[-J^{-1}\frac{\delta_{i2}}{Fr^2}+D_{\mathrm{I}}(\tilde{u}_i^1)\right]$$

$$\tilde{u}_i^2-\hat{u}_i^2=\gamma_2\frac{R_i(\tilde{\phi}^2)}{\tilde{\varrho}^2J^{-1}}+\zeta_1\frac{R_i(\tilde{\phi}^1)}{\tilde{\varrho}^1J^{-1}}$$

Step 3:

$$(J^{-1}-\alpha_3\Delta t D_{\mathrm{I}})\frac{(\hat{u}_i^3-\tilde{u}_i^2)}{\Delta t}=\gamma_3[C(\tilde{u}_i^2)+D_{\mathrm{E}}(\tilde{u}_i^2)+T_i(\tilde{d}^2)]+\zeta_2[C(\tilde{u}_i^1)+D_{\mathrm{E}}(\tilde{u}_i^1)+T_i(\tilde{d}^1)]+2\alpha_3\left[-J^{-1}\frac{\delta_{i2}}{Fr^2}+D_{\mathrm{I}}(\tilde{u}_i^2)\right]$$

$$u^{n+1}-\hat{u}_i^3=\gamma_3\frac{R_i(\phi^{n+1})}{\varrho^{n+1}J^{-1}}+\zeta_2\frac{R_i(\tilde{\phi}^2)}{\tilde{\varrho}^2J^{-1}}$$

The coefficients α, γ, ζ are reported in Reference [16] and in literature cited therein. In the above equations, for the sake of clarity, a compact notation is used to represent the convective terms, the diffusive terms and the surface tension contributions:

$$C(u_i) = -\frac{\partial}{\partial \xi_m}(U_m u_i) \tag{18}$$

$$D_{\mathrm{I}}(u_i) = \frac{1}{\varrho Re}\frac{\partial}{\partial \xi_m}\left(\mu G^{ml}\frac{\partial u_i}{\partial \xi_l}\right) \quad m = l \tag{19}$$

$$D_{\mathrm{E}}(u_i) = \frac{1}{\varrho Re}\frac{\partial}{\partial \xi_l}\left(\mu G^{ml}\frac{\partial u_i}{\partial \xi_l} + \mu B^{mkji}\frac{\partial u_j}{\partial \xi_k}\right) \quad m \neq l \tag{20}$$

$$T_i(d) = -\frac{\kappa}{\varrho We^2}\frac{\partial}{\partial \xi_m}\left(J^{-1}\frac{\partial \xi_m}{\partial x_i}H(d)\right) \tag{21}$$

while

$$R_i(f) = -\frac{\partial}{\partial \xi_m}\left(J^{-1}\frac{\partial \xi_m}{\partial x_i}f\right) \tag{22}$$

is the gradient operator in generalized co-ordinates.

In the corrector steps, ϕ is the pressure corrector term which is found by enforcing the continuity of the velocity field at the end of the substep, [16, 17]. The procedure is as follows: once the intermediate velocity field is found, say $\hat{u}_i^l$, the fluxes associated to this velocity field ($\hat{U}_m^l$) are computed by (14) at the mid point of the cell faces through a QUICK scheme. In terms of fluxes, the corrector step can be written as

$$\tilde{U}_m^l - \hat{U}_m^l = -\gamma_l \Delta t\left(\frac{G^{mj}}{\tilde{\varrho}^l}\frac{\partial \tilde{\phi}^l}{\partial \xi_j}\right) - \zeta_{l-1}\Delta t\left(\frac{G^{mj}}{\tilde{\varrho}^{l-1}}\frac{\partial \tilde{\phi}^{l-1}}{\partial \xi_j}\right) \tag{23}$$

so that, by applying the continuity (13) to $\tilde{U}_m^l$, the following Poisson equation for the pressure corrector is obtained:

$$\frac{\partial}{\partial \xi_m}\left(\frac{G^{mj}}{\tilde{\varrho}^l}\frac{\partial \tilde{\phi}^l}{\partial \xi_j}\right) = \frac{1}{\Delta t}\frac{\partial \hat{U}_m^l}{\partial \xi_m} - \frac{\zeta_{l-1}}{\gamma_l}\frac{\partial}{\partial \xi_m}\left(\frac{G^{mj}}{\tilde{\varrho}^{l-1}}\frac{\partial \tilde{\phi}^{l-1}}{\partial \xi_j}\right) \tag{24}$$

When the velocity field is assigned throughout the boundary of the computational domain, (23) provides Neumann boundary conditions for the solution of the Poisson equation (24).

The pressure corrector term is related to the pressure field by the following equation:

$$R_i(\tilde{p}_{\mathrm{F}}^l) = (\tilde{\varrho}^l J^{-1} - \alpha_l \Delta t D_{\mathrm{I}})\left(\frac{R_i(\tilde{\phi}^l)}{\tilde{\varrho}^l J^{-1}}\right) \tag{25}$$

but, since the solution of this equation is not straightforward, usually, an approximate pressure field is obtained as [18]:

$$R_i(\tilde{p}_{\mathrm{F}}^l) \simeq R_i(\tilde{\phi}^l) \Rightarrow \tilde{p}_{\mathrm{F}}^l = \tilde{\phi}^l + O(\Delta t) \tag{26}$$

The system of equation discussed above is spatially discretized by a central finite difference approach, second-order accurate. As already stated, a second-order upwind scheme (QUICK) is used to evaluate volume fluxes at the cell faces. These latter are needed both to compute convective terms (18) and to evaluate the source term for the Poisson (24). At each substep of the Runge–Kutta scheme, the momentum equation is solved by using an approximate factorization approach of the diffusive part, as suggested in Reference [17]. The time step is chosen so that the Courant number is always smaller than $\sqrt{3}$ and the stability constraint required by surface tension is satisfied [13]

$$\Delta t < We \sqrt{\frac{(1+\varrho_a)}{4\pi} \Delta x^3}$$

Since not all the viscous contributions are treated implicitly, some limitation to the time step can be required.

A multigrid technique is adopted for the solution of the Poisson equation for the pressure corrector term, which is the most expensive part of the computational procedure. A corrector scheme is used for restriction and prolongation [19] and an LSOR method is employed as high frequency smoother. Since metric quantities and fluid properties appear into the coefficients of the Poisson equation, a simple average of the metric and of the distance function is used in the restriction phase.

3.2. Free surface capturing via level-set technique

In the level-set technique, fluid properties are related to the signed normal distance from the interface $d(\mathbf{x},t)$ which, at $t=0$, is initialized by assuming $d>0$ in water, $d<0$ in air and $d=0$ at the interface [9]. For the generic fluid property f it is assumed

$$f(d) = \begin{cases} f_a & \text{if } d < -\delta \\ \dfrac{f_w + f_a}{2} + \dfrac{f_w - f_a}{2} \sin\left(\dfrac{\pi d}{2\delta}\right) & \text{if } |d| < \delta \\ f_w & \text{if } d > \delta \end{cases} \tag{27}$$

Here δ is the half-width of a transition region introduced to smooth the jump in the fluid properties and to avoid problems when evaluating derivatives of fluid properties. Usually, it is at least 4 times the cell size [1]. The same smoothing is also applied to the Heaviside function [14], thus obtaining

$$H_\delta(d) = \begin{cases} 0 & \text{if } d < -\delta \\ \dfrac{1}{2} + \dfrac{1}{2} \sin\left(\dfrac{\pi d}{2\delta}\right) & \text{if } |d| < \delta \\ 1 & \text{if } d > \delta \end{cases} \tag{28}$$

During the motion, the distance is transported by the flow, that is the equation

$$\frac{\partial d}{\partial t} + \mathbf{u} \cdot \nabla d = 0 \tag{29}$$

is integrated to update the distribution of the function d and then to follow the interface as the level set $d=0$. The integration is carried out with the three-steps Runge–Kutta by using the same discretization scheme adopted for the convective terms, thus obtaining

$$\hat{d}^l = \tilde{d}^{l-1} + \gamma_l \Delta t C(\tilde{d}^{l-1}) + \zeta_{l-1} \Delta t C(\tilde{d}^{l-2}) \tag{30}$$

with $\tilde{d}^0 \equiv d^n$, $\tilde{d}^3 \equiv d^{n+1}$ and

$$C(\tilde{d}^l) = -\frac{\partial}{\partial \xi_m}(\tilde{U}_m^l \tilde{d}^l)$$

When studying free surface waves, disturbances propagate towards the lateral boundaries of the computational domain and, to avoid spurious reflections, a numerical beach model is introduced in the transport equation (29) as suggested by Vogt and Larsson [20]:

$$\frac{\partial d}{\partial t} = -\mathbf{u} \cdot \nabla d - \nu(d + x_2) \tag{31}$$

where x_2 is the vertical axis oriented upward, $x_2=0$ being the still water level. The model is applied onto two beach regions close to the lateral bounds of the computational domain. The damping coefficient ν is zero at the inner limit of the beaches and grows quadratically toward the boundaries.

To keep constant the width of the jump region, the distance function is periodically reinitialized by computing, at each cell centre, the minimum distance from the interface. Several efficient procedures have been developed to this aim by Russo and Smereka [21], Strain [22] and Sussman and Fatemi [23], among others. In the present work, a direct approach is used which computes the exact distance from the reconstructed interface [24]. Attention being mainly focused on two-dimensional applications, the computational effort requested by a direct reinitialization of the distance is not prohibitive.

The reinitialization starts from the reconstruction of the interface location as the contour $\hat{d}^j=0$. Being the distance function defined at the centre of the cell, a system of staggered cells is considered for the reconstruction (Figure 2). First of all, the occurrence of interface passages within each of the staggered cells is investigated. In a first-order interpolation scheme, a cell crossed by the interface is easily identified by the occurrence of changes in the sign of the distance function at the vertices: in two dimensions, only one or two crossing are allowed (Figure 3). The intersection of the interface with the faces of the staggered cells is then found by linear interpolation. When a single crossing occurs, in order to improve the accuracy in the representation of the interface, a further point is introduced by using a bilinear representation of the distance function within the staggered cell. In this way, for each staggered cell crossed by the interface, the level $\hat{d}^j=0$ is represented by two segments. At the end of the reconstruction, the distance is reinitialized as the normal distance from the closest interface segment, thus obtaining $\tilde{d}^l$. For the sake of saving the computational effort, the reinitialization of the distance function is carried out only in a narrow band about the interface and at the boundaries of the computational domain [25].

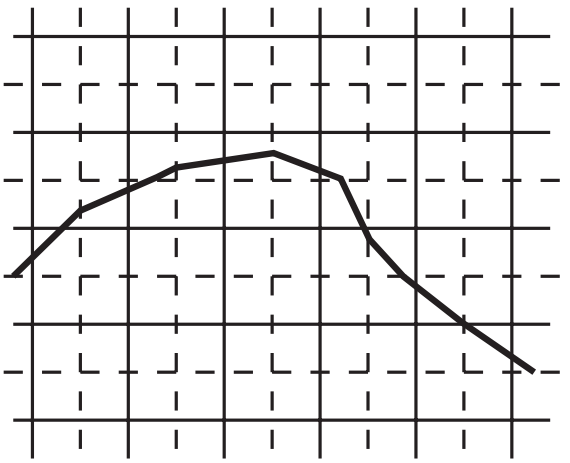

Figure 2. Sketch of the staggered layout used for the reconstruction of the free surface location.

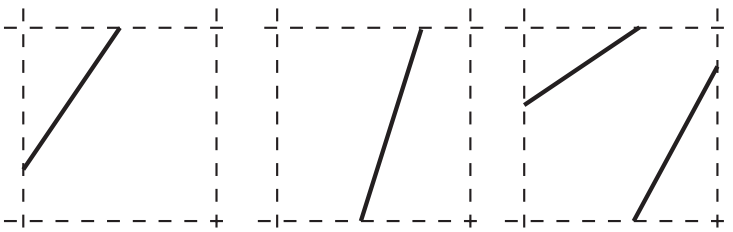

Figure 3. Possible crossing configuration of the interface through a cell.

3.3. Solution of the potential flow in the bottom region

The flow in the bottom region is described in terms of a boundary integral representation of the velocity potential φ. At any point $\mathbf{x}$ inside Ω_B it is written as

$$\varphi(\mathbf{x}) = \int_{\partial\Omega_B} \left[\frac{\partial\varphi}{\partial n}(\mathbf{y}) G(\mathbf{x}-\mathbf{y}) - \varphi(\mathbf{y}) \frac{\partial G}{\partial n}(\mathbf{x}-\mathbf{y}) \right] \mathrm{d}s(\mathbf{y}) \tag{32}$$

where $G(\mathbf{x}-\mathbf{y})$ is the free space Green's function for the Laplace operator and $\mathbf{n}$ is the unit normal vector oriented inward.

To obtain the distribution of the velocity potential inside the domain, φ and its normal derivative all along $\partial\Omega_B$ have to be found, hence (32) is written as $\mathbf{x} \to \partial\Omega_B$, thus obtaining

$$\frac{1}{2}\varphi(\mathbf{x}) = \int_{\partial\Omega_B} \left[\frac{\partial\varphi}{\partial n}(\mathbf{y}) G(\mathbf{x}-\mathbf{y}) - \varphi(\mathbf{y}) \frac{\partial G}{\partial n}(\mathbf{x}-\mathbf{y}) \right] \mathrm{d}s(\mathbf{y}) \tag{33}$$

The solution of this boundary integral equation is numerically achieved by discretizing the boundary with straight line panels and assuming that the velocity potential and its normal derivative are constant along each panel and equal to the value they take at the midpoint.

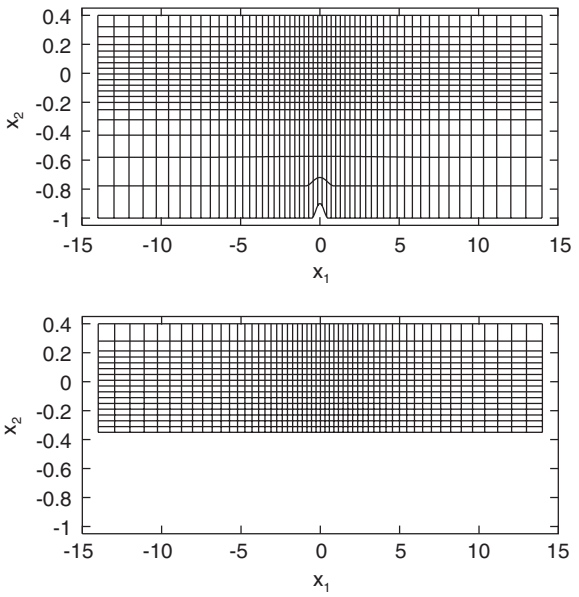

Figure 4. Computational grids used in the FNS (*top*) and domain decomposition (*bottom*) simulations of the wavy flow generated by a bottom bump. For clarity, only one every fourth grid point is shown.

The solution of the linear system provides the velocity potential on the bottom surface and along the two lateral boundaries. Once the boundary integral equation is solved, the velocity potential, and hence the velocity field at any point $\mathbf{x} \in \overline{\Omega_B}$ can be computed, thus providing the boundary condition for the Navier–Stokes solver in the free surface domain Ω^F. It is worth to notice that, when the velocity field is assigned at the boundary of the Navier–Stokes domain, the compatibility constraint

$$\int_{\Gamma^F} \mathbf{u}^F \cdot \mathbf{n} \, ds = 0$$

is enforced at each time step. This condition stems from the continuity equation and from the boundary conditions applied along the remaining part of the boundary of the upper subdomain $\partial\Omega_I^F \cup \partial\Omega_O^F \cup \partial\Omega_T^F$. A similar constraint is enforced along Γ_B in the NT approach, when the normal velocity component is used as boundary condition for the Laplace equation in Ω^B.

The distribution of panels at matching line, Γ^B or Γ in the NT or DT case, respectively, coincides with the bottom faces of the row of the cells $j = jo$ of the Navier–Stokes solver, being $jo = 1$ if no overlapping is used. In the NT approach, when overlapping is necessary, variables at the midpoint of the panels are evaluated by averaging the values at the two contiguous cells at $j = jo$ and $jo - 1$. In the DT approach overlapping of the domains is not used and the values of the pressure at $j = 1$ and at the ghost points, introduced to enforce boundary condition (23) for the Poisson equation (24), are used.

When studying the wavy flow produced by the submerged hydrofoil, a quasi-steady Kutta condition is enforced at the trailing edge. This is done by introducing a vortex line which goes from the leading to the trailing edge. Its circulation is computed so that the flow at the

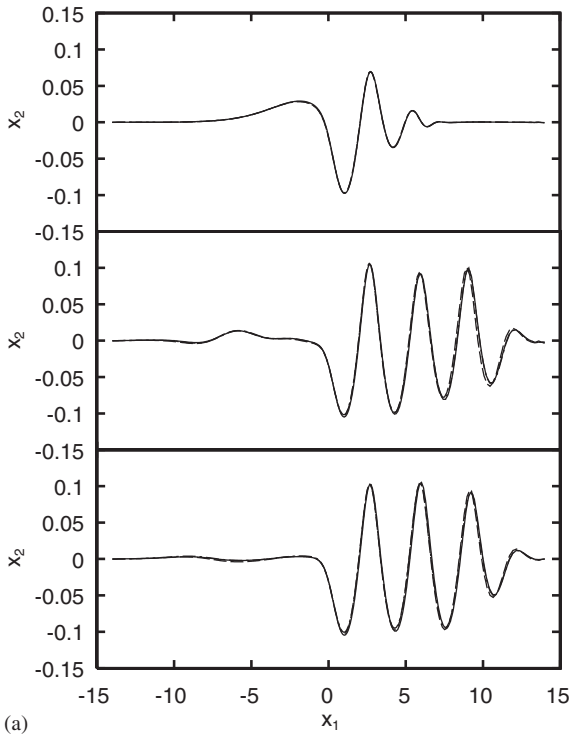

Figure 5. Comparisons among the FNS (*solid line*), the DT (*dashed line*) and the NT (*dash–dotted line*) for the wavy flow generated by a bottom bump. The comparison is established in terms of the wave elevation (*a*), horizontal (*b*) and vertical (*c*) velocity components and pressure field (*d*) at the matching line. Three different times are shown: 10 (*top*), 50 (*middle*), 150 (*bottom*).

trailing edge is directed along the chord of the profile. The use of this quasi-steady Kutta condition in an unsteady free surface problem can be accepted on the base of the rather poor effect that the vorticity shedded by the hydrofoil plays on the free surface, at least on the first wavelengths, the rising motion of the vortex structures being very slow and possibly affecting the free surface dynamics only in the far field.

4. NUMERICAL RESULTS

In the following, the developed domain decomposition approaches are applied to two different problems.

For validation purposes, the wavy flow generated past a bump placed on the bottom of a free surface channel is simulated, and the results obtained with the domain decomposition are compared with those obtained by solving the Navier–Stokes equations in the whole fluid domain (FNS hereinafter). Qualitative and quantitative analysis of the errors are performed in terms of the wave profiles and of the variables exchanged at the matching line. Dependency of the solution on the extension of the overlapping and on the position of the matching is also verified.

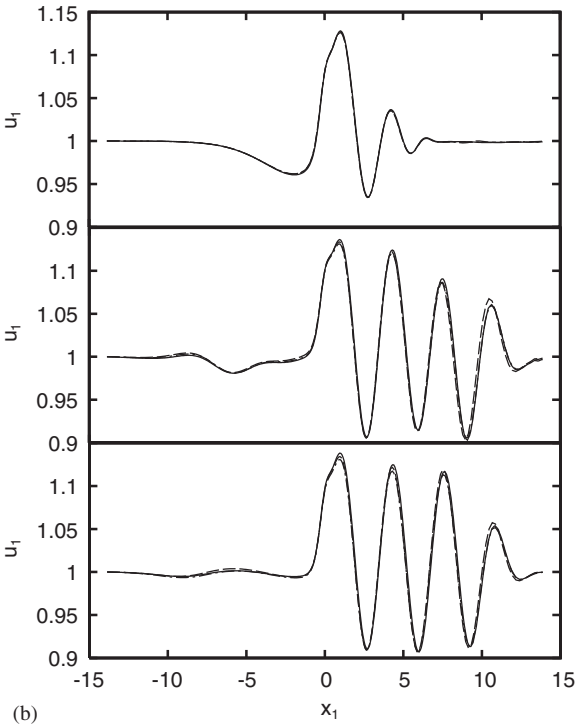

Figure 5. (*continued*)

As a second type of flow, extensively studied in literature, both numerically [26] and experimentally [27–29], the wave pattern produced by a submerged hydrofoil, in breaking and non-breaking condition, is studied. This case is simulated with DT approach and results are compared with experimental data and inviscid numerical results.

In all the computations, density and viscosity ratios between the two fluids are assumed to be equal to their effective values for air and water.

Independently of the strategy adopted for the coupling, the convergence of the subiterations is established in terms of the velocity assigned as boundary condition to the Navier–Stokes solver, which is evaluated as

$$r = \frac{\|\mathbf{u}^{k+1} - \mathbf{u}^{k}\|}{\|\mathbf{u}^{k+1}\|}$$

In the calculation showed below, solution is reiterated up to $r < 10^{-8}$ is reached.

4.1. Flow about a bottom bump: validation and verification of the coupling strategies

The domain decomposition approaches are applied to the case of the wavy flow past a bump, which is assumed to suddenly start at the speed $V = (-1, 0)$, while the water is assumed to be initially at rest. The simulations are carried out at $Re = 10\,000$, $Fr = 0.707$, $We = 10$.

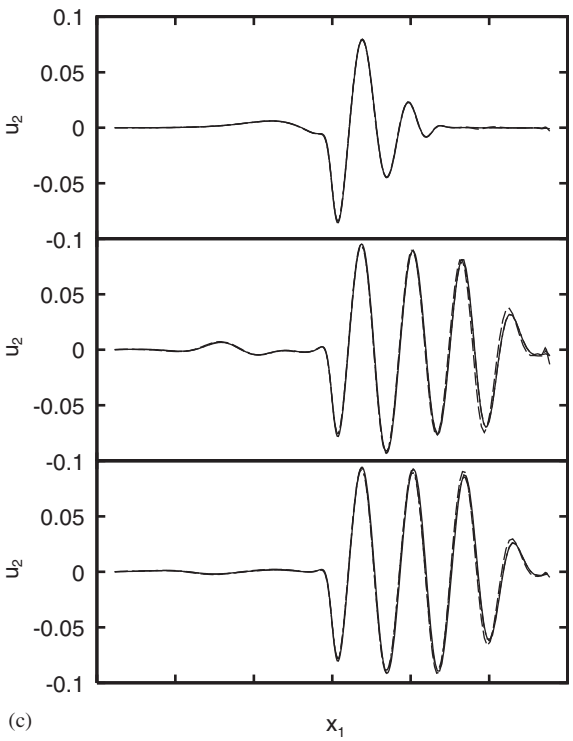

Figure 5. (*continued*)

The geometry of the problem is the following: the horizontal axis x_1 is oriented from the left to the right, while x_2 is oriented upward (Figure 4) with $x_2=0$ denoting the still water level. The shape of the bottom is described by the equation

$$x_2(x_1)=-0.9-0.8x_1^2+1.6x_1^4$$

for $|x_1|<0.5$, and it is $x_2(x_1)=-1$ elsewhere. The top boundary is located in the air region at $x_2=0.4$. The horizontal extension of the computational domain is in the range $-14<x_1<14$. With reference to Equation (31), two damping zones are introduced for $|x_1|\in(8,14)$, where $v=2$ at the boundaries of the domain. In the computations, half of the width of the transition region is $\delta=0.04$.

In order to have a fair comparison between results obtained by the domain decomposition approaches, a free slip boundary condition is applied on the bottom of the channel when solving the FNS problem. As a consequence, although the grid employed in the FNS computation is of the body fitted type, cells are not clustered close to the bottom (Figure 4). Instead, to correctly follow the formation and propagation of the free surface waves, both the FNS and the domain decomposition computational grids are vertically clustered near the still water level, $\Delta x_2=0.01$, and horizontally clustered about the centre of the bump, with the horizontal

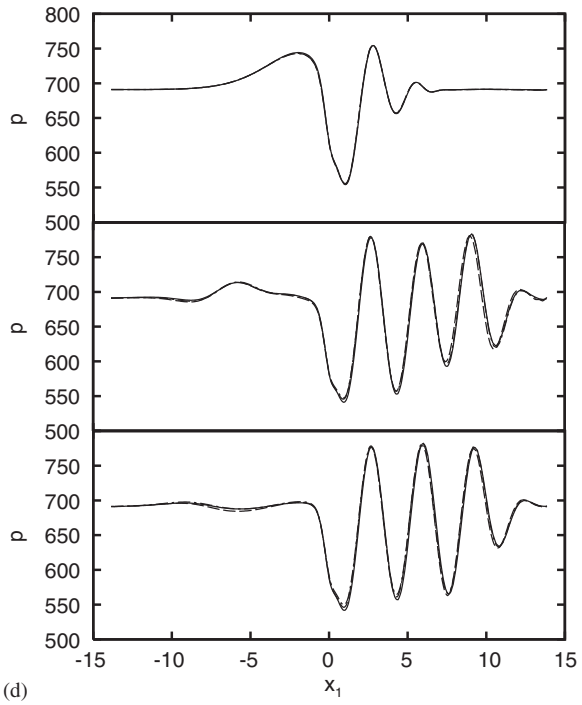

(d)

Figure 5. (*continued*)

grid spacing ranging from $\Delta x_1 = 0.07$ about $x_1 = 0$ up to $\Delta x_1 \approx 0.27$ at the two ends of the computational domain.

Of course, when using the domain decomposition approach, the number of grid points depends on the location of the matching line and on the extension of the overlapping region. These two aspects are discussed in the following. Here, results with the NT approach are presented as computed with Γ^F at $x_2 = -0.35$ with an extension of the overlapping equal to 0.15, while DT results are obtained with Γ at $x_2 = -0.35$. For these two cases the grid used in the free surface region has 220×64 grid points, against 220×76 of the corresponding FNS calculation.

In Figure 5 the comparison among the FNS, NT and DT approaches is performed reporting at different times the wave elevation, the two velocities components u_1, u_2 and the pressure p at the matching line. The motion the bump induces the establishment of a wavy flow. The free surface is characterized by an initially unsteadiness that almost vanishes after $t = 40$, except for some residual oscillations due to the impulsive start and to the weak reflections from the numerical beaches. The agreement between the two domain decomposition approaches and the FNS is rather satisfactory, both being able to correctly follow the process of formation and propagation of the waves. The time evolution of velocities and pressure is substantially the same: as the solution advances in time and fills the computational domain, a weak disagreement appears, slowly growing until the wave is fully developed ($t \approx 40$), remaining constant afterwards.

Table I. Relative errors and subiterations for NT and DT strategies.

DD type	ε_{u_1}	ε_{u_2}	ε_p	Subits*.
DT	$5.53\,10^{-3}$	0.1156	$8.42\,10^{-3}$	3.3
NT	$4.51\,10^{-3}$	0.0800	$6.69\,10^{-3}$	12

*The averaged number of subiterations required at each substep is reported.

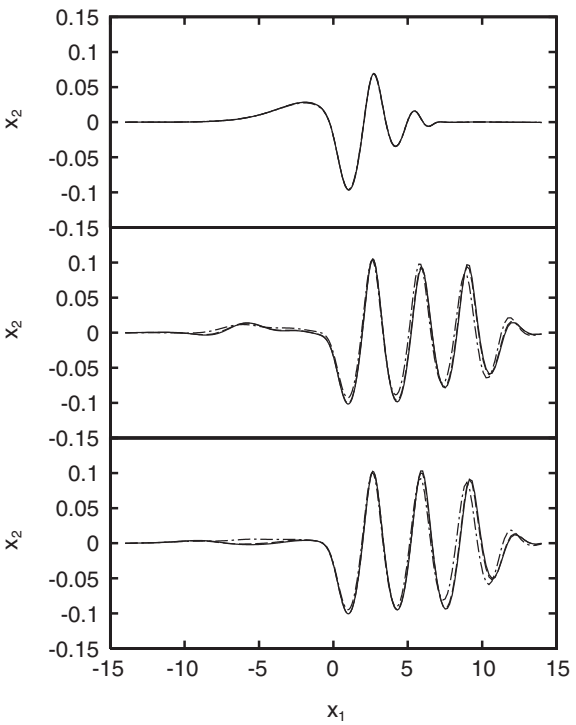

Figure 6. Effects of the overlapping extension on the NT approach on the free surface profile: 0.15 (*solid line*), 0.10 (*dashed line*), 0.05 (*dash–dotted line*). Three different times are shown: 10 (*top*), 50 (*middle*), 150 (*bottom*).

To have a quantitative measure of the relative error with respect to the FNS results, the following estimates:

$$\varepsilon_f = \frac{\|f_{\mathrm{FNS}} - f_{\mathrm{DD}}\|}{\|f_{\mathrm{FNS}}\|}$$

are introduced and evaluated for u_1, u_2, p at the matching line at $t = 150$, and reported in Table I along with the average number of subiterations. When comparing the two domain decomposition approaches, the NT one exhibits a smaller error while DT is significantly faster in terms of the number of subiterations required to achieve convergence at each substep.

Table II. NT: effect of the overlapping extension on relative errors and subiterations.

Overlapping	ε_{u_1}	ε_{u_2}	ε_p	Subits.
0.15	$4.51\,10^{-3}$	0.0800	$6.69\,10^{-3}$	12
0.10	$6.11\,10^{-3}$	0.1085	$8.75\,10^{-3}$	16
0.05	$1.75\,10^{-2}$	0.3361	$2.67\,10^{-2}$	16

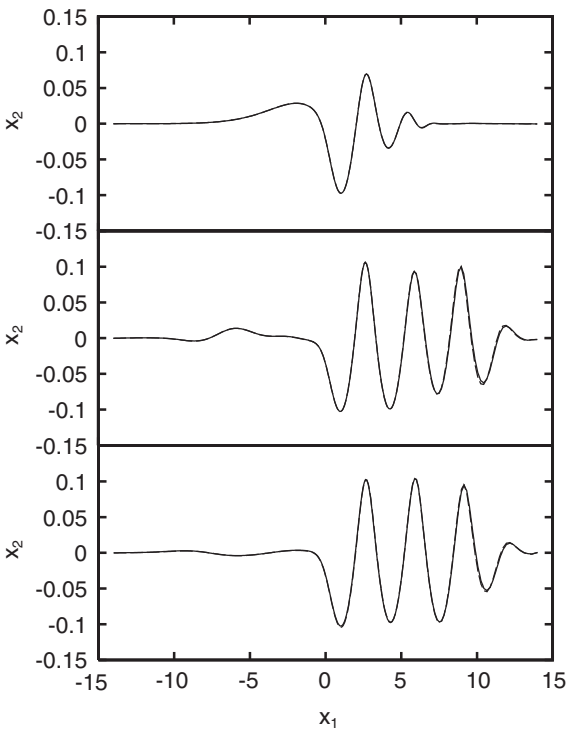

Figure 7. Effects of the position of the matching line on the DT approach on the free surface profile: $x_2(\Gamma) = -0.35$ (*solid line*), $x_2(\Gamma) = -0.19$ (*dashed line*). Three different times are shown: 10 (*top*), 50 (*middle*), 150 (*bottom*).

Results show that the vertical velocity component suffers from the largest relative error while much smaller discrepancies are obtained in terms of horizontal velocity component and pressure field. Concerning this point, it is worth to notice that, since the vertical velocity is oscillating about a zero value, the error is significantly induced by the phase shift, as it can be noticed in Figure 5(c). However, in absolute terms, u_2 is of the order of one-tenth of the reference velocity V. Hence, from this viewpoint, the absolute error of the u_2 is essentially of the same order of the other variables.

To analyse the dependency of the NT results on the extension of the overlapping, computations have been repeated with two different position of the matching line Γ^B, namely

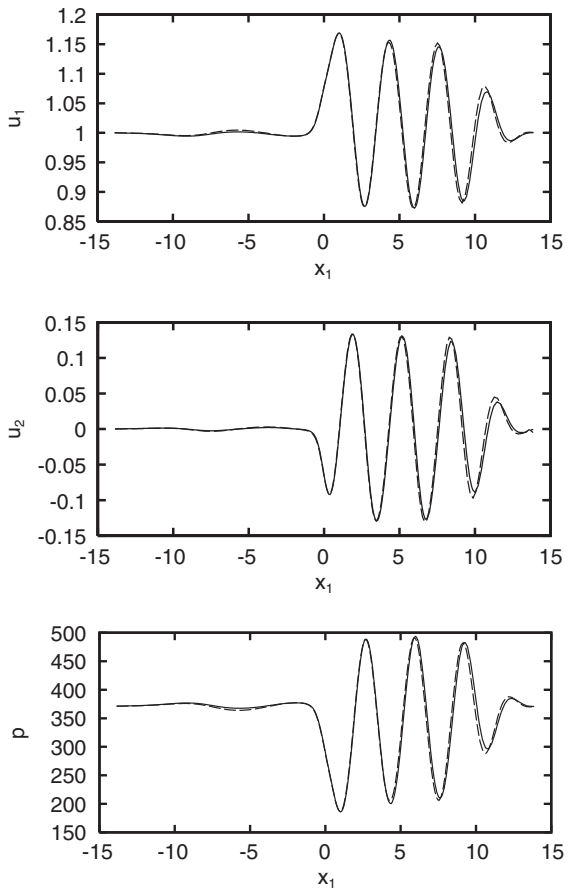

Figure 8. Effects of the position of the matching line on the DT approach on the exchanged variable: FNS (*solid line*), DT with $x_2(\Gamma) = -0.19$ (*dashed line*) at $t = 150$.

0.10, 0.05. Results with the three values of the overlapping are shown in Figure 6 and the errors with respect to the FNS simulation are reported in Table II. It can be noticed that the use of a too small overlapping extension, such as 0.05, yields an unsatisfactory result while differences between the cases at 0.15 and 0.10 are essentially negligible. Obviously as the overlapping extension reduces, the number of the subiterations required to achieve convergence is increased.

It has to be pointed out that, at least in principle, the Schwarz alternating approach should perform almost independently of the overlapping extension, although an increase in the number of the subiteration has to be expected [11]. However, in the present method, this characteristic is inhibited by the particular choice of the numerical approach employed to solve the flow in the inviscid subdomain Ω^B. As a matter of fact, the flow in the bottom region is described in terms of a zero-order panel method which does not provide an accurate reconstruction of the velocity field at distances much smaller than the panel length. As a consequence, the

Table III. DT: effect of several parameters on relative errors and subiterations.

$x_2(\Gamma)$	Grid	CFL	ε_{u_1}	ε_{u_2}	ε_p	Subits.
-0.35	220×64	1.8	$5.53\,10^{-3}$	0.1156	$8.42\,10^{-3}$	3.3
-0.19	220×48	1.8	$8.48\,10^{-3}$	0.1417	$2.43\,10^{-2}$	3.3
-0.19^*	220×48	0.45	$7.20\,10^{-3}$	0.1290	$2.12\,10^{-2}$	3
-0.19^*	440×96	1.8	$6.52\,10^{-3}$	0.1054	$1.86\,10^{-2}$	3

*Comparison is established with the FNS computation that uses the same parameters.

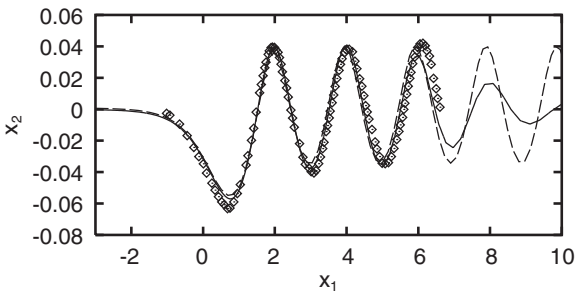

Figure 9. Free surface profile generated by a submerged hydrofoil. DT (*solid line*), BEM (*dashed line*), experimental data by Duncan ($\diamond$).

overlapping extension 0.05, being always smaller than the panel length, which goes from 0.07 at the centre, to 0.27 at the two far boundaries, leads to some differences in the velocity field on Γ^F, resulting in a progressive worsening of the solution, as the sequence in Figure 6 shows.

From this standpoint, the Dirichlet coupling performs much better. Actually, in this coupling strategy, the overlapping is not needed, and the velocity field to be passed to the Navier–Stokes solver can be directly evaluated from the values of the velocity potential and of its normal derivative at the collocation points, which are much more accurate.

Beside that, not needing an overlapping, is it possible to further reduce the size of the viscous subdomain Ω^F. Indeed, the location of the matching surface is a matter of a trade-off between the attempt of reducing at the most the subdomain where the complex model has to be solved and the risk of getting too close to the free surface, i.e. the boundary of the potential subdomain has to be located in a region where rotational effects are negligible. Here, Γ is moved from $x_2 = -0.35$ up to $x_2 = -0.19$, which is quite close to the free surface, being the throat of the first wave located at $x_2 \simeq -0.13$ and the thickness of the transition region has also to be considered. Results in terms of free surface elevation are shown in Figure 7 versus those obtained by using $x_2(\Gamma) = -0.35$ whereas, in Figure 8, the velocity components and the pressure at the matching line are compared with those provided by the FNS. It can be noted that, in spite of the narrow region used for the free surface subdomain, the agreement with the FNS is good as also indicated by the relative errors reported in Table III.

As a verification of the accuracy, other calculations are carried out by using a smaller CFL constraint and a more refined grid obtained by halving the original one. Relative error in

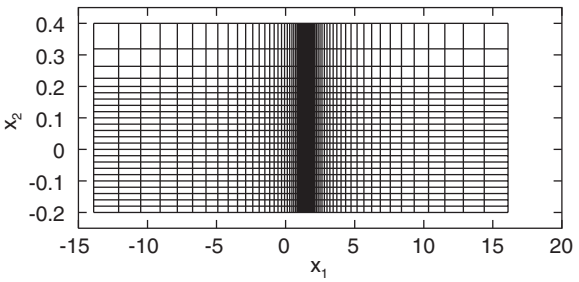

Figure 10. Computational grid used for the study of the wavy flow in breaking condition generated by a submerged hydrofoil. For clarity, only one every eighth grid point is shown.

both cases does not change significantly, see Table III, thus suggesting that differences are essentially due to the simplified model used in the bottom subdomain.

The rationale for this test case was the validation of the domain decomposition strategies versus FNS calculations. However, for this case, the rather simple grid required by the FNS calculation does not make evident the advantage that can be achieved by using the domain decomposition approach. In the next section, the model so far discussed is applied to a much more complex configuration. In this case, the advantage in using the heterogeneous domain decomposition comes from the possibility of excluding a large portion of grid points from the viscous subdomain (Figure 14).

4.2. Wavy flow past a hydrofoil

The domain decomposition approach is applied to study the wavy flow generated by a submerged hydrofoil moving beneath the free surface. In this case, a correct description of the viscous flow past the hydrofoil would require a highly refined body fitted grid. Likely, the pressure field produced by the hydrofoil, responsible for the generation of the wave motion, can be efficiently predicted by a potential flow model, provided a Kutta condition is applied at the trailing edge, hence substituting the expensive FNS solver with a fast BEM solution.

Firstly, the regular wavy flow generated by an NACA 0012 hydrofoil 5° angle of attack is numerically computed by the domain decomposition and results are compared with those obtained by using the boundary element approach in the whole fluid domain and with experimental data by Duncan [27]. According to the experimental data, the non-dimensional submergence of the hydrofoil is 1.285 and the bottom of the channel is located at $x_2 = -2.1477$, being the chord of the hydrofoil the reference length. A 256×96 grid, suitably clustered about the hydrofoil and the first two downstream wavelength, is used in the viscous subdomain, while about 700 panels are used in the description of the flow in the bottom subdomain. The matching line and the top boundary are located at $x_2 = -0.2$ and 0.4, respectively.

The Froude and Weber numbers are the same as the experimental ones, being $Fr = 0.567$ and $We = 42$, respectively, while a smaller value of the Reynolds number, $Re = 10^4$, is used in the numerical calculations. In order to reduce reflections from the side boundaries of the domain and to fasten the achievement of a steady solution, a sinusoidal ramp is adopted which accelerate the body from the rest up to the final speed, that is reached at $t = 50$. In Figure 9, the free surface elevation at $t = 100$ is compared with the corresponding inviscid solution and

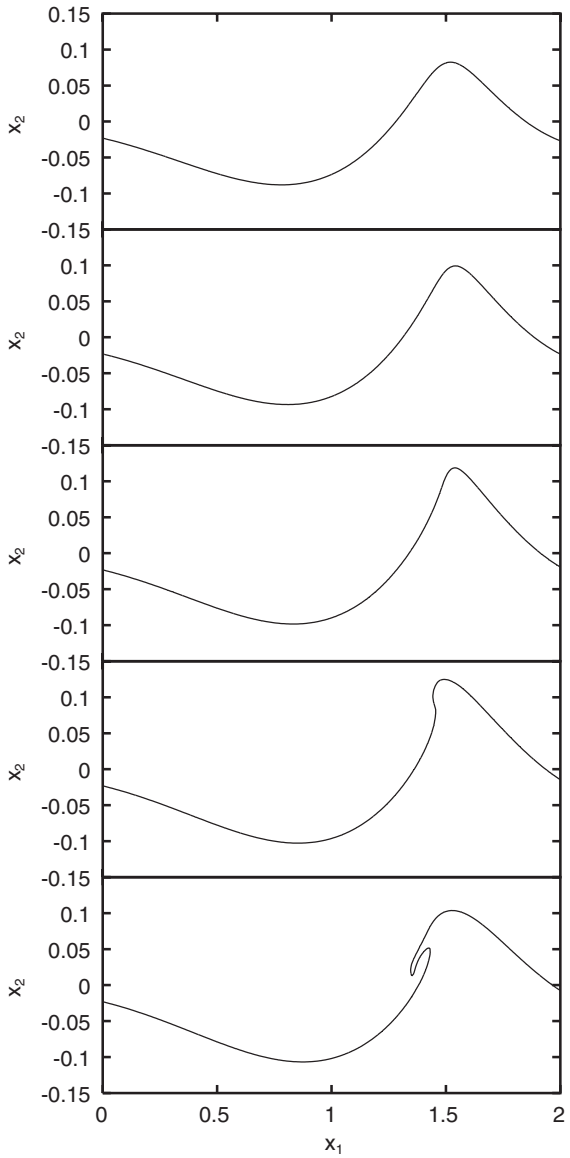

Figure 11. Free surface evolution about the first wave crest showing the breaking onset. Times are $39, 40, 41, 42, 43$ from top to bottom.

the experimental results by Duncan [27]. Up to $x_1 = 5$ the agreement is rather good, while, due to the large horizontal grid spacing adopted in the following region, a strong wave damping takes place after $x_1 = 6$.

A second calculation is carried out for a non-dimensional submergence of the hydrofoil of 0.783, for which an intense spilling breaker has been experimentally observed [27]. To

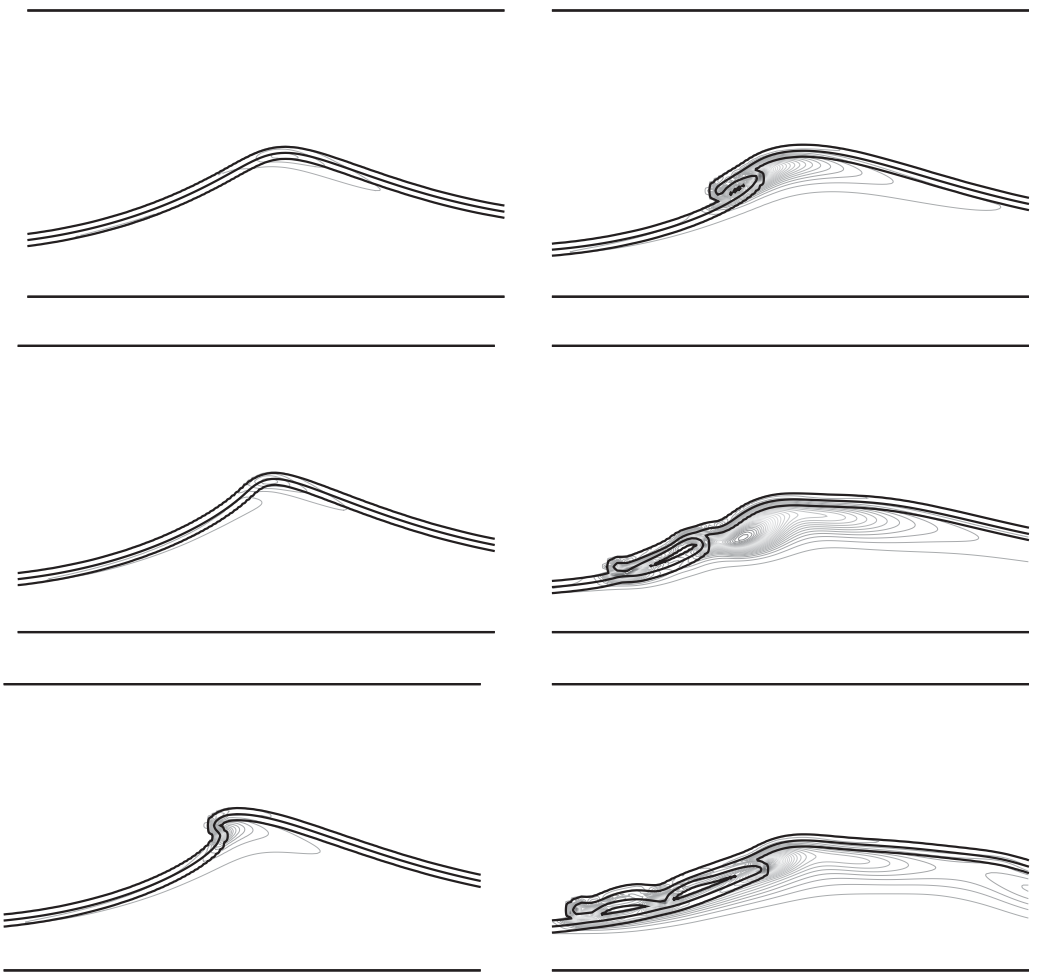

Figure 12. Evolution of the free surface and of the vorticity $\times$ density contours during the breaking onset and after the plunging. Times are $40, 41, 42$ from top to bottom on the left and $43, 44, 45$ from top to bottom on the right. Three density levels (20, 500, 980) are shown to display the interface location and the thickness of the transition region.

resolve the larger velocity gradients expected in this case, numerical calculations are carried out at $Re = 1000$ on a 512×192 grid (Figure 10).

In Figure 11, the wave elevation about the first crest is shown at different times of the accelerating ramp. The sequence clearly shows the steepening of the wave which eventually gives rise to the formation of a thin jet which propagates in the forward direction and plunges onto the forward face of the wave.

More insights about the effects of the breaking development on the flow pattern are shown in Figure 12, where vorticity $\times$ density contours are shown together with three density contour lines $(20, 500, 980)$ identifying the free surface. The quantity vorticity $\times$ density is introduced

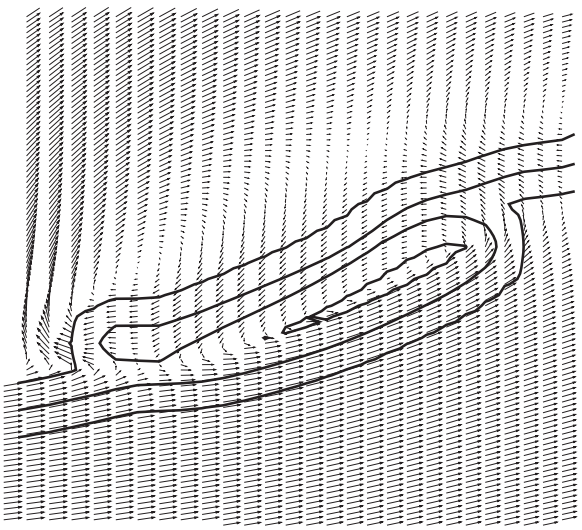

Figure 13. Detailed view of the velocity field at $t=44$ about the breaking region. High velocity gradients occur at the impact point and all along the contact line between the forward face of the wave and the fluid portion sliding above.

to highlight the flow pattern in water, disregarding the flow field in air. Similarly to the sequence in Figure 11, a steep wave is initially formed. Successive steps are the formation of a bulge and the development of a jet. The plunging of the latter on the forward face of the wave is followed by the formation of a new jet, again impacting on the water, hence propagating the breaking front further upstream.

The same sequence points out the development of the shear layer initially induced by the bulge formation. As a consequence of the impact of the falling jet, two layers of fluid, having large differences in the velocity field, came into contact (see Figure 13), moving upstream the starting point of the shear layer. The shear layer is then convected downstream by the flow, as it is shown in Figure 14, thus slackening the flow of the uppermost water layers resulting, in a fixed frame of reference, in the generation of a surface current [28]. Finally, this figure makes also evident the advantages of using the domain decomposition approach. Indeed, the domain in which the solution of the Navier–Stokes equation is required is confined in a narrow region about the interface.

5. CONCLUSIONS

A heterogeneous domain decomposition method has been used to face the complex free surface flow induced by wave breaking occurrence. A two-fluid incompressible Navier–Stokes approach has been adopted to compute the flow in the free surface region with a level-set technique employed for the interface capturing, while the potential flow model has been assumed in the deeper region. Two different strategies of coupling have been developed and tested against the corresponding fully viscous and fully inviscid results and with experimental

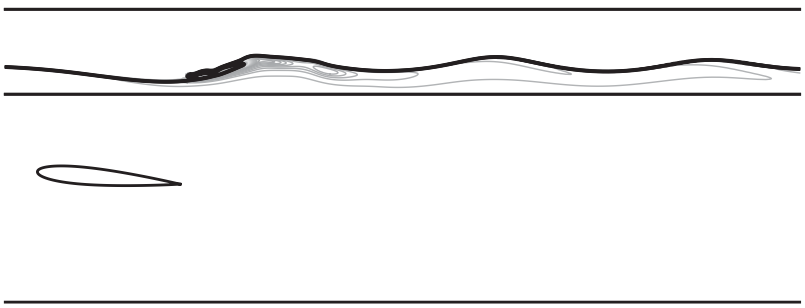

Figure 14. View of the central region of the fluid domain. The picture, which refers to $t=45$, shows the downstream propagation of the shear layer induced by the breaking region. The three horizontal lines represent the top boundary, the matching line and the bottom of the channel, respectively, underlying that the solution of the Navier–Stokes equations may be confined to a portion which can be as small as 30% of the whole fluid domain.

data. For validation the wavy flow generated by a bottom bump and by a submerged hydrofoil in non-breaking conditions have been numerically simulated. Results obtained with the domain decomposition approach have been found in a good qualitative and quantitative agreement with the reference solutions.

The method has been finally applied to the study of the wave breaking flow generated by a hydrofoil moving close to the free surface. In this case the domain decomposition approach, focusing the computational resources in the description of the most interesting part of the flow domain, has allowed the description of all the relevant phenomena generated by the breaking onset.

ACKNOWLEDGEMENTS

This work has been partially supported by the *Office of Naval Research*, under grant N000140010344, though Dr Pat Purtell and partially supported by the *Ministero delle Infrastrutture e dei Trasporti* in the frame of the INSEAN Research Plan 2000-02. Authors wish to thank Dr Douglas Dommermuth for the useful discussions had during his visit at INSEAN and Prof. Alfio Quarteroni for the suggestion he gave them in developing the coupling strategies.

REFERENCES

1. Iafrati A, Di Mascio A, Campana EF. A level-set technique applied to unsteady free surface flows. *International Journal for Numerical Methods in Fluids* 2001; **35**:281.
2. Longuet-Higgins MS. Shear instability in spilling breakers. *Proceedings of the Royal Society of London*, Series A 1994; **446**:399.
3. Duncan JH. Spilling breakers. *Annual Review Fluid of Mechanics* 2001; **33**:519.
4. Longuet-Higgins MS, Cokelet ED. The deformation of steep surface waves on water. I. A numerical method of computation. *Proceedings of the Royal Society of London*, Series A 1976; **350**:1.
5. New AL, McIver P, Peregrine DH. Computations of overturning waves. *Journal of Fluid Mechanics* 1985; **150**:233.
6. Scardovelli R, Zaleski S. Direct numerical simulation of free surface and interfacial flow. *Annual Review of Fluid Mechanics* 1999; **31**:567.
7. Tahara Y, Stern F, Rosen B. An interactive approach for calculating ship boundary layers and wakes for non zero Froude number. *Journal of Computational Physics* 1992; **98**:33.
8. Campana EF, Di Mascio A, Esposito PG, Lalli F. Viscous-inviscid coupling in free surface ship flows. *International Journal for Numerical Methods in Fluids* 1995; **21**:699.

9. Sussman M, Smereka P, Osher SJ. A level set approach for computing solutions to incompressible two-phase flow. *Journal of Computational Physics* 1994; **114**:146.
10. Smith BF, Bjorstad PE, Gropp WD. Domain decomposition. *Parallel Multilevel Methods for Elliptic Partial Differential Equations*. Cambridge University Press: Cambridge, MA, 1996.
11. Quarteroni A, Valli A. *Domain Decomposition Methods for Partial Differential Equations*. Oxford University Press: Oxford, UK, 1999.
12. Iafrati A, Campana EF. Unsteady free surface flow around hydrofoils. *Proceedings of BEM20*, *Orlando* (*USA*), *1998*. In *Boundary Elements XX*, Kassab A, Brebbia CA, Chopra M (eds). Computational Mechanics Publications: UK, 1998.
13. Brackbill JU, Kothe DB, Zemach C. A continuum method for modeling surface tension. *Journal of Computational Physics* 1992; **100**:335.
14. Sussman M, Puckett G. A coupled level-set and volume-of-fluid method for computing 3D and axisymmetric incompressible two-phase flows. *Journal of Computational Physics* 2000; **162**:301.
15. Zang Y, Street RL, Koseff JR. A non-staggered grid, fractional step method for time-dependent incompressible Navier–Stokes equations in curvilinear coordinates. *Journal of Computational Physics* 1994; **114**:18.
16. Rai MM, Moin P. Direct simulations of turbulent flow using finite-difference schemes. *Journal of Computational Physics* 1991; **96**:15.
17. Kim J, Moin P. Application of a fractional-step method to incompressible Navier–Stokes equations. *Journal of Computational Physics* 1985; **59**:308.
18. Rosenfeld M, Kwak D, Vinokur M. A fractional step solution method for the unsteady incompressible Navier–Stokes equations in generalized coordinate system. *Journal of Computational Physics* 1991; **94**:102.
19. Brandt A. Guide to multigrid development. In *Multigrid Methods*, Hackbush W, Trottenberg U (eds). Springer, Berlin, Germany, 1992.
20. Vogt M, Larsson L. Level set methods for predicting viscous free surface flows. *Proceedings of the 7th International Conference on Numerical Ship Hydrodynamics*, Nantes, France, 1999.
21. Russo G, Smereka P. A remark on computing distance functions. *Journal of Computational Physics* 2000; **163**:55.
22. Strain J. Tree methods for moving interfaces. *Journal of Computational Physics* 1999; **151**:616.
23. Sussman M, Fatemi E. An efficient, interface-preserving level-set redistancing algorithm and its application to interfacial incompressible fluid flow. *SIAM Journal on Scientific Computing* 1999; **20**(4):1165.
24. Sussman M, Dommermuth D. The numerical simulation of ship waves using cartesian grid methods. *Proceedings of the 23rd ONR Symposium on Naval Hydrodynamics*, Val de Reuil, France, 2000.
25. Sethian JA. *Level Set Methods and Fast Marching Methods*. Cambridge University Press: Cambridge, UK, 1999.
26. Hino T, Martinelli L, Jameson A. A finite volume method with unstructured grid for free surface flow simulations. *Proceedings of the 6th International Conference on Numerical Ship Hydrodynamics*, Iowa, USA, 1993.
27. Duncan JH. The breaking and non-breaking wave resistance of a two-dimensional hydrofoil. *Journal of Fluid Mechanics* 1983; **126**:507.
28. Battjes JA, Sakay T. Velocity field in a steady breaker. *Journal of Fluid Mechanics* 1981; **111**:421.
29. Mori KH. Sub-breaking waves and critical condition for their appearance. *Journal of Society of Naval Architecture Japan* 1986; **159**:1.

